



# Visualizing features with wide-field volumetric OCT angiography

TRISTAN T. HORMEL,<sup>1</sup> GUANGRU B. LIANG,<sup>1</sup>  XIANG WEI,<sup>1,2</sup>   
YUKUN GUO,<sup>1,2</sup>  MIN GAO,<sup>1,2</sup>  JIE WANG,<sup>1</sup>  DAVID HUANG,<sup>1</sup>   
STEVEN T. BAILEY,<sup>1</sup> THOMAS S. HWANG,<sup>1</sup> AND YALI JIA<sup>1,2,\*</sup> 

<sup>1</sup>Casey Eye Institute, Oregon Health and Science University, Portland, OR 97239, USA

<sup>2</sup>Department of Biomedical Engineering, Oregon Health and Science University, Portland, OR 97239, USA

\*jiaya@ohsu.edu

**Abstract:** Optical coherence tomography (OCT) and its extension OCT angiography (OCTA) have become essential clinical imaging modalities due to their ability to provide depth-resolved angiographic and tissue structural information non-invasively and at high resolution. Within a field of view, the anatomic detail available is sufficient to identify several structural and vascular pathologies that are clinically relevant for multiple prevalent blinding diseases, including age-related macular degeneration (AMD), diabetic retinopathy (DR), and vein occlusions. The main limitation in contemporary OCT devices is that this field of view is limited due to a fundamental trade-off between system resolution/sensitivity, sampling density, and imaging window dimensions. Here, we describe a swept-source OCT device that can capture up to a  $12 \times 23$ -mm field of view in a single shot and show that it can identify conventional pathologic features such as non-perfusion areas outside of conventional fields of view. We also show that our approach maintains sensitivity sufficient to visualize novel features, including choriocapillaris morphology beneath the macula and macrophage-like cells at the inner limiting membrane, both of which may have implications for disease.

© 2024 Optica Publishing Group under the terms of the [Optica Open Access Publishing Agreement](#)

## 1. Introduction

Several leading causes of vision loss, including age-related macular degeneration (AMD) [1], diabetic retinopathy (DR) [2], and branch retinal vein occlusions [3] afflict the retina and choroid. A variety of features and biomarkers are used to diagnose and stage these diseases [4–6]. Characterization and quantification of these pathologic features can improve our understanding of disease pathophysiology and help inform therapeutic research. Important biomarkers, e.g. neovascularization in proliferative DR [7], can occur anywhere in the retina, requiring large fields of view for detection. Other features, e.g. intraretinal microvascular abnormalities [8,9], are best characterized volumetrically as their (3-dimensional) location relative to retinal tissue structure. High-resolution imaging is also required to detect small pathologies such as microaneurysms [10–12]. This set of requirements is difficult to meet, and highly detailed retinal and choroidal imaging has consequently relied on ex vivo histology. However, histology also has important limitations. Ex vivo approaches are inherently of limited utility in clinical practice. And even from a research perspective, histology is not ideal since it is not applicable to longitudinal studies, which means that the relationship between pathologic features and disease progression must be inferred by analyzing cohorts. For similar reasons, histology cannot capture dynamic processes such as cell translocation or blood flow. An in vivo approach that meeting the above requirements would be advantageous for both research and clinical practice. We also desire a technology that could be useful for screening (i.e., a non-invasive, low-cost procedure), both to achieve the most advantageous clinical outcomes and to aid data collection for studies of early stages of disease development.

Optical coherence tomography (OCT) [13] is the most promising technology for meeting these needs with a single procedure. An interferometric imaging modality, OCT is non-invasive, depth-resolved, high-resolution, and inexpensive [14]. These capabilities have already positioned OCT as an essential technology for imaging key treatment indicators in AMD (exudation) and DR (edema) [15–21]. Furthermore, by using motion contrast between successive scans to highlight blood flow, OCT angiography (OCTA) allows OCT devices to achieve vascular imaging down to the capillary scale while inheriting the main advantages of OCT reflectance imaging, including volumetric data acquisition and non-invasive procedures [22–25].

Ideally, coupled OCT and OCTA imaging would provide this rich volumetric information throughout the entire retina and choroid. However, contemporary devices fail to achieve this feat due to several technological hurdles, including the presence of projection artifacts, signal attenuation in posterior anatomic slabs, incomplete flow detection, and the difficulty of reconciling high-resolution imaging with large fields of view [26–30]. In this study, we investigated the ability of a custom-designed swept-source single-shot OCTA system to allay these issues in order to provide high-quality imaging of eyes affected by AMD, branch retinal vein occlusion, and DR, each of which is a prevalent cause of vision loss. In particular, we explored the ability of this device to characterize features (e.g. choriocapillaris vascular morphology) that have proven difficult to assess with contemporary commercial devices [31–33].

## 2. Methods

### 2.1. Study population and inclusion criteria

We recruited healthy participants and participants with AMD, branch retinal vein occlusion, and diabetes from Oregon Health and Science University (OHSU) and obtained informed written consent under a protocol in accordance with the Declaration of Helsinki and compliant with the Health Insurance Portability and Accountability Act of 1996. The institutional review board of OHSU approved the protocol. Participants underwent a full clinical examination, including an Early Treatment of Diabetic Retinopathy Study (ETDRS) protocol as well as imaging with the study device.

### 2.2. System hardware specifications

Our swept-source OCTA device (Fig. 1) uses a 500-kHz A-line rate vertical-external-cavity surface-emitting laser (VECSEL) with a 1060-nm peak wavelength and 100-nm bandwidth (Thorlabs, NJ). It has a theoretical axial resolution of 5- $\mu\text{m}$  in air with a 230- $\mu\text{m}$  depth of focus. Laser power was measured to be 2.68 mW at the cornea, meeting ANSI safety requirements [34]. This is relatively low compared to contemporary commercial systems; for example, DREAM OCT (Intalight) and PlexElite (Zeiss) use 3.4 and 5 mW light sources at the same center wavelength, respectively. System sensitivity was measured to be 102-dB at 0.2-mm with a roll-off of 1-dB over 4-mm of imaging depth [35]. A self-built Mach-Zender interferometer was used as a sampling clock for the laser. We use post-correction to compensate for dispersion at large scanning angles [36], but we note that aberrations due to the eye can still be an issue when imaging in the periphery (see discussion).

Optical resolution for posterior segment imaging in OCT systems is determined by the focal spot size on the retina. Commercial systems use a small ( $\approx 1\text{-mm}$ ) collimated beam in part because this avoids defocus due to astigmatism, but this beam size results in focal spot sizes of 15-20- $\mu\text{m}$ , which is larger than the width of the smallest capillaries ( $\approx 5\text{-}10\text{-}\mu\text{m}$ ). [37] Consequently, capillaries appear wider in standard OCTA than is anatomically correct. This is problematic for imaging vascularly dense tissues such as the choriocapillaris since capillary broadening can prevent morphological details [38] (e.g. vessel connectivity) from being quantified or observed.

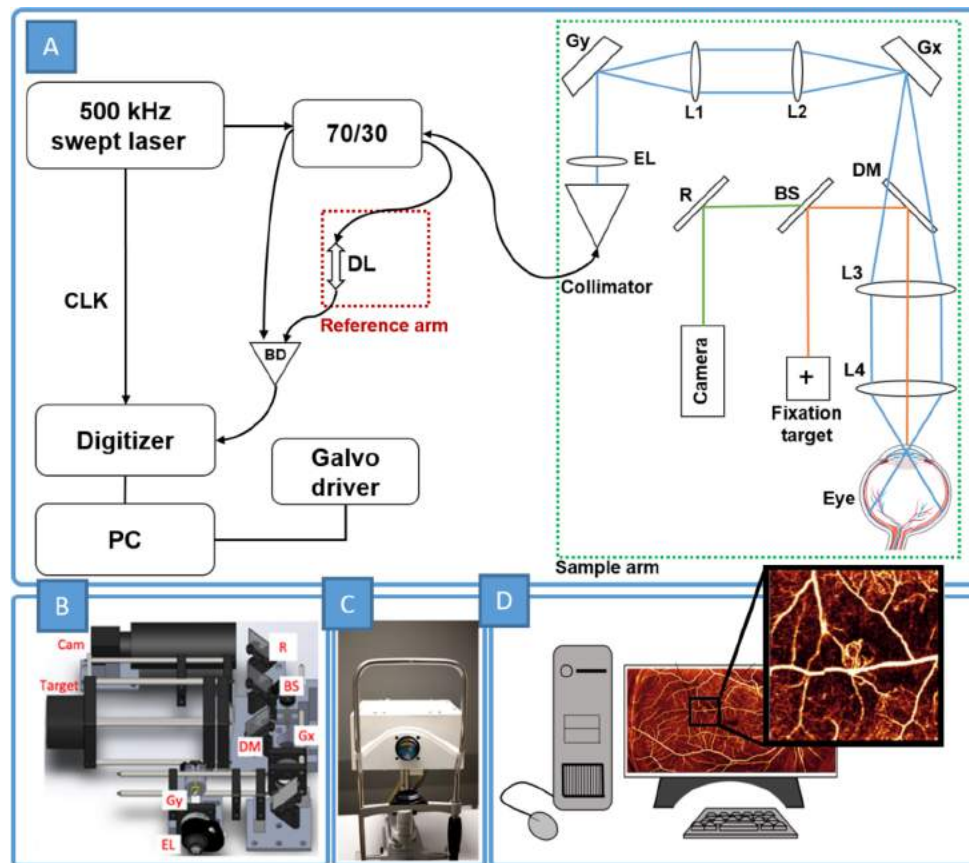


**Fig. 1. System design.** (A) Schematic. Light from a 500-kHz swept source laser is split by a 70/30 beam splitter, with 30% traveling to the sample arm (green box). In the sample arm galvo motors position the sample beam in the eye, with an optical relay composed of lenses  $L$  preventing vignetting artifacts. The 40-mm effective focal length lens  $L1$  provides a 75-degree field of view in the posterior segment. A fixation target and camera are also incorporated in the sample arm optical path. Reference arm a length is adjusted by a delay line. System output is converted to an electronic signal by a balanced detector and digitized so that it can be processed in a computer.  $L1$ : 40 mm effective focal length lens,  $L2$ : 100 mm effective focal length lens,  $L3$  and  $L4$ : 33 mm effective focal length lenses,  $Gx$ : galvo driver for positioning along the  $x$  direction,  $Gy$ : galvo driver for positioning along the  $y$  direction,  $BS$ : 50:50 beam splitter,  $R$ : silver mirror,  $DM$ : dichroic mirror,  $EL$ : electric lens,  $DL$ : delay line,  $BD$ : balanced detector,  $CLK$ : built-in sampling clock,  $PC$ : personal computer. (B) CAD rendered model (Solidworks, Dassault Systèmes). (C) Photo of the system showing its patient interface. (D) Illustration showing wide-field OCTA on a proliferative diabetic retinopathy patient being reviewed on the system's monitor. The optical design of our system enables not only the large FOV but also the single-capillary level resolution.

Our system uses a 2.2 mm collimated beam ( $1/e^2$  beam waist) in order to achieve a spot size of 10- $\mu\text{m}$  on the retina, substantially improving transverse resolution relative to commercial devices.

Vignetting is a common artifact in OCTA imaging. This issue is particularly acute when imaging over larger fields of view. A major source of vignetting in OCTA is misalignment of the sample arm focal spot between the separate X-axis and Y-axis mirrors in conventional galvo scanners. This means that if the X-axis focal point is aligned on the pupil, the Y-axis might not be

(and vice-versa). In misaligned regions the sample beam can be blocked by the iris. For narrow scanning angles then misalignment is generally not a large concern because the scanning angle is far from the iris and will not be blocked. For widefield scanning though vignetting can cause major artifacts. Our system avoids vignetting by using an optical relay consisting of a 4f system (two lens groups separated by the sum of their focal lengths) to project the galvo X-axis on to the center of the galvo Y-axis, thereby avoiding beam wandering [30]. This sample arm design and the swept-source laser are combined in the OCTA system as shown in Fig. 1. An electric lens adjusts for diopter variation among imaging subjects.

### 2.3. Data acquisition

The split-spectrum amplitude-decorrelation [24] algorithm was used to generate OCTA signal through three repeat scans from the same slow-axis positions. Wide-field  $12 \times 23$  scans were sampled at a density of 1206 A-lines per B-scan and 2304 B-scans per volumes, which equates to a transverse pixel dimension of  $10 \mu\text{m}$ . By comparison, Nyquist sampling would use  $2400 \times 4600$  sampling points over the same volume; we do not sample at this density in order to keep scan times reasonable. Broadly, a scan takes about a minute with our device, but this number is highly contingent on the number of motion tracking adjustments required to remove artifacts. Signal generation, however, is accomplished in real time in order to provide operator feedback to help improve image quality. We adjust transverse sampling density for smaller images; the resultant pixel sizes are noted in the figure descriptions.

### 2.4. En face image generation

Creating en face images requires projection over bounded sub-volumes corresponding to anatomically appropriate regions of interest such as plexuses, vascular complexes, or the choriocapillaris. We use a guided bi-directional graph search method [39] integrated into our COOL-ART reading software platform that automatically identifies tissue boundaries by finding the shortest path between two points weighted by the gradient of the reflectance image. The points used in the search (the guidance point array) were determined by first finding the boundary between the inner limiting membrane boundary and the vitreous. This was performed by adding the gradient map to the cross-sectional image and searching for the first non-zero pixel from the top of each A-line. A second guidance point array corresponding to the ellipsoid zone (or cone inner segment/outer segment junction) is constructed by locating the minimum of the gradient image, which occurs at that location. Additional guidance point arrays for other boundaries can then be obtained from gradient maps bounded between the ellipsoid zone and the inner limiting membrane. Operating on these guidance point arrays, the bidirectional graph search can iteratively remove outliers along the anatomically correct layer boundaries. This approach can fail, particularly in scans exhibiting advanced pathologic features such as retinal fluid, which can cause the gradient to vanish and the gradient-based graph search to fail. In such cases, COOL-ART includes the ability to manually correct mis-segmented boundaries manually, thereby avoiding segmentation artifacts. Once slab boundaries have been identified, we obtain the en face angiogram using maximum value projection for the flow signal in the relevant slab; this produces angiograms with a better signal-to-noise ratio and contrast than alternatives such as mean value projection [40].

### 2.5. Artifact correction

In addition to blood flow, several other sources of motion exist in the eye. Microsaccades in particular are detrimental to OCTA image quality because rapid repositioning of the eye manifests as bright strips in which the real flow signal can be obscured. Additionally, even with the innovations discussed above to improve scan acquisition rate, for wide-field images total acquisition time can still be long enough that imaging subjects will need to blink. We use a



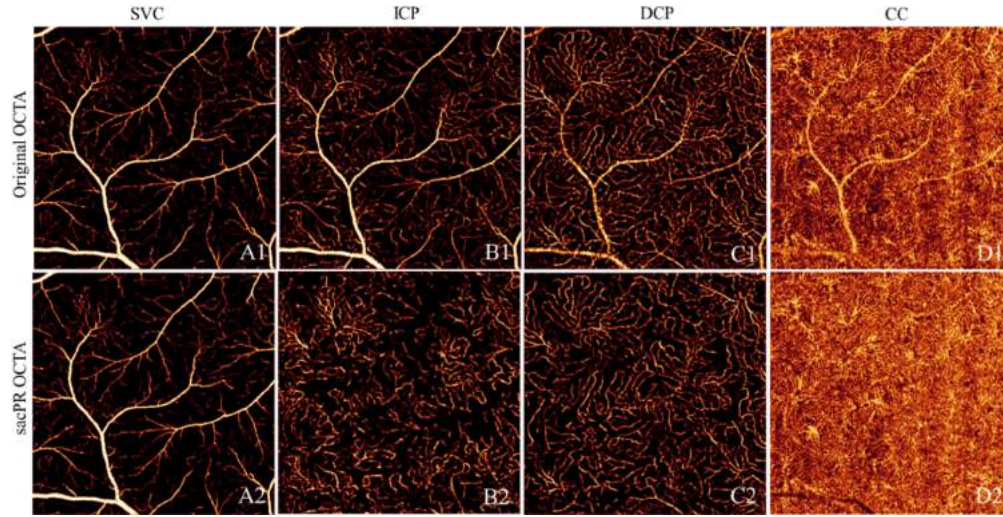


**Fig. 2. Signal attenuation compensated projection artifact removal.** Row 1: original, uncorrected OCTA en face images of the superficial vascular complex (SVC, A1), intermediate capillary plexus (ICP, A2), deep capillary plexus (DCP, A3), and choriocapillaris (CC, A4). Strong projection artifacts beneath the large SVC vessels are visible in each of the ICP, DCP, and CC images. Row 2: corresponding signal attenuation compensated projection resolved (sacPR) OCTA. The prominent projection artifacts are removed in these images. In addition to removing projection artifacts, this approach also leaves in situ vessels intact, as demonstrated by a lack of over-processing producing artificial gaps in the vasculature or truncated vessels.

self-navigation motion correction system [41] to remove these and other artefacts that cause large disruptions in image quality. For a grid of decorrelation values  $D(x, y, z)$  this system is based on an instantaneous motion strength index (IMSI) defined by

$$\text{IMSI}(D_{x=x_b}) = \frac{\text{std}(D_{x=x_b})}{\text{mean}(D_{x=x_b})}$$

where  $D_{x=x_b}$  is distribution of decorrelation values at in the cross-sectional scan located at  $x = x_b$  and  $\text{std}[\cdot]$  is the standard deviation. When the IMSI value exceeds a threshold, the system will automatically trigger a rescan at that location so that data from that region is not lost or disrupted. In the current work the IMSI threshold was set to an empirically determined value of  $\text{IMSI} = 0.25$ .

Another major concern in OCTA is projection artifacts. These artifacts reproduce flow patterns from anterior vascular layers in posterior layers, making the identification of pathology like choroidal neovascularization more difficult. Projection artifacts should be removed volumetrically so that both cross-sectional and en face images can be used. In this work we use a volumetric signal attenuation compensated projection artifact removal technique (Fig. 2) [42]. In this approach, voxel values are scaled according to their distance from in situ flow in order to help assess the flow signal originating at a certain location free of corruption from projection artifacts. The method also includes an additional procedure for removing shadows underneath large vessels, which are especially problematic since they can produce both large projection artifacts on the retinal pigment epithelium and large reductions in the reflectance signal in the retina.

## 2.6. Image enhancement

Even with the high-resolution device used in this work capillaries can be difficult to distinguish in vascularly dense tissue. This is due to a combination of factors including noise and the width

of capillaries being similar to the device's beam spot size on the retina. We use a deep-learning image reconstruction model to further enhance the appearance of the vessels in the retinal angiograms in this work (Fig. 3) [43]. This algorithm was trained by requiring the corresponding regions of output  $6 \times 6$ -mm en face angiograms to match higher-resolution angiograms acquired with  $3 \times 3$ -mm field of view. Although the network was trained on  $6 \times 6$ -mm angiograms, it also improved  $3 \times 3$ -mm and wide-field angiogram image quality in terms of noise intensity, contrast, and vessel connectivity. Applying this model to the images in this work led to more visually clear capillaries. Because the network has not been tested on choriocapillaris images, it was not applied to the OCTA images of this region.

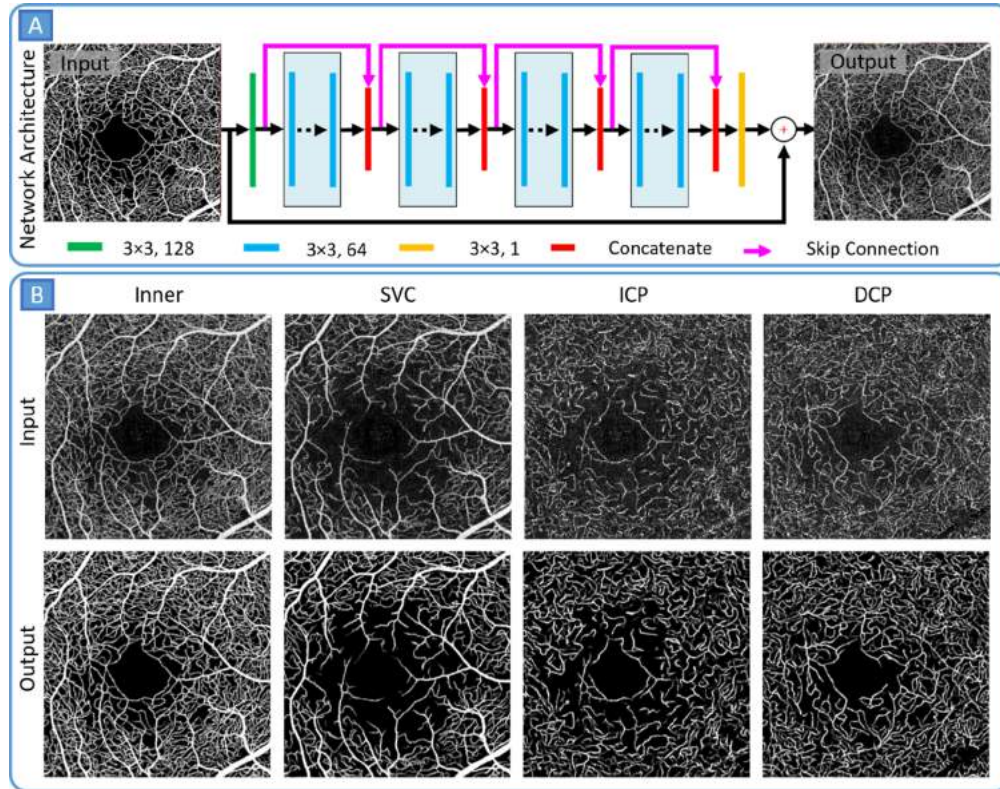


**Fig. 3. Deep-learning-based angiogram reconstruction.** Top row: raw OCTA angiograms of the superficial vascular complex (SVC), intermediate capillary plexus (ICP), and deep capillary plexus (DCP), and the projection across each of these layers (inner). Middle row: network architecture. Bottom row: reconstructed angiograms. The reconstruction process removes much of the background, making vessels and their morphology easier to identify. The deep learning network used to achieve the reconstruction was trained to up-sample image quality using low density/high density scans of the same eye. In these  $3 \times 3$ -mm images the transverse pixel resolution is  $4 \mu\text{m}/\text{pixel}$ .

### 3. Results

#### 3.1. Coupled structural and angiographic OCT of the retina and choroid

Our approach enables detailed imaging of structural features and vasculature throughout the retina and choroid (example from a healthy eye in Fig. 4). Several technical features are notable in these images:



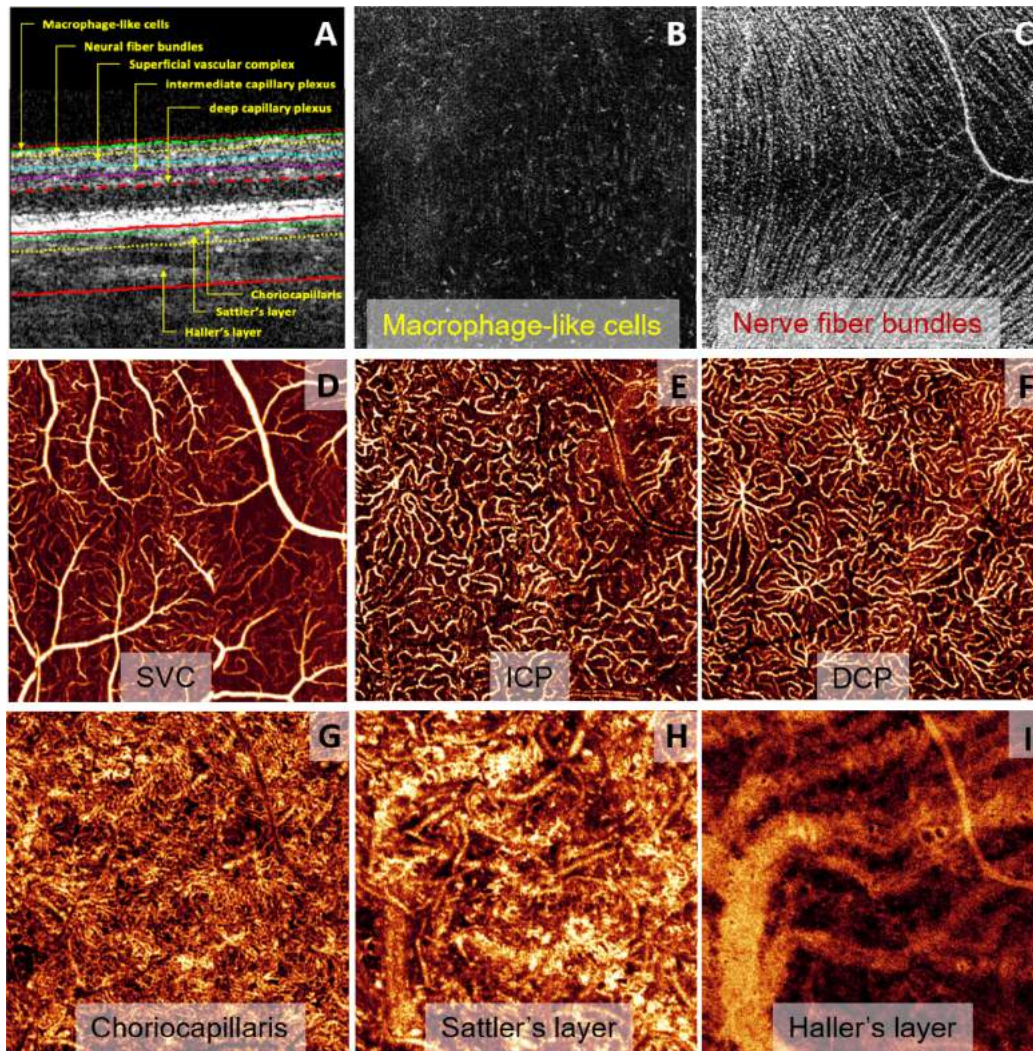


**Fig. 4. Comprehensive high-resolution OCT angiography in a healthy eye.** All images were captured from a  $3 \times 3$ -mm region temporally adjacent to the macula. (A) Cross-sectional OCT with colored lines indicating segmented anatomic slab boundaries, with text and arrows to show the boundaries used to generate en face images in (B-I). (B) Macrophage-like cells are visible as bright dots adjacent to the inner limiting membrane in this structural en face OCT image. (C) Individual nerve fibers are visible in the structural channel, with their orientation clearly discernable. (D) Superficial vascular complex (SVC) with both large vessels and capillaries seen with exquisite detail with OCT angiography (OCTA). (E) OCTA of the intermediate capillary plexus (ICP) and (F) deep capillary plexus (DCP). The lobular nature of the DCP is clearly visible thanks to the improved transverse resolution of our system. (G) OCTA of the choriocapillaris with individual capillaries visible. The fenestrated appearance rendered here is similar to the choriocapillaris appearance with electron microscopy (cf. Figure 6). (H) Sattler's layer with intermediate-sized choroidal vessels. (I) Haller's layer, showing large vessels. Vessels in (I) and (H) were captured in the structural channel due to the fast flow speed in these vessels, which are difficult to image with interscan times appropriate for retinal flow. Each of these images was compiled from a single shot procedure at  $4\text{-}\mu\text{m}$  / pixel transverse sampling density.



**High transverse resolution.** Capillaries are well-resolved in the retinal vascular layers and choroid (Fig. 4–6) to be resolved. In particular, the lobular nature of the deep capillary plexus network [44] is readily visible using our device (Fig. 5). With our approach, the choriocapillaris edges are precisely demarcated and inter-capillary spaces are apparent (Fig. 6).

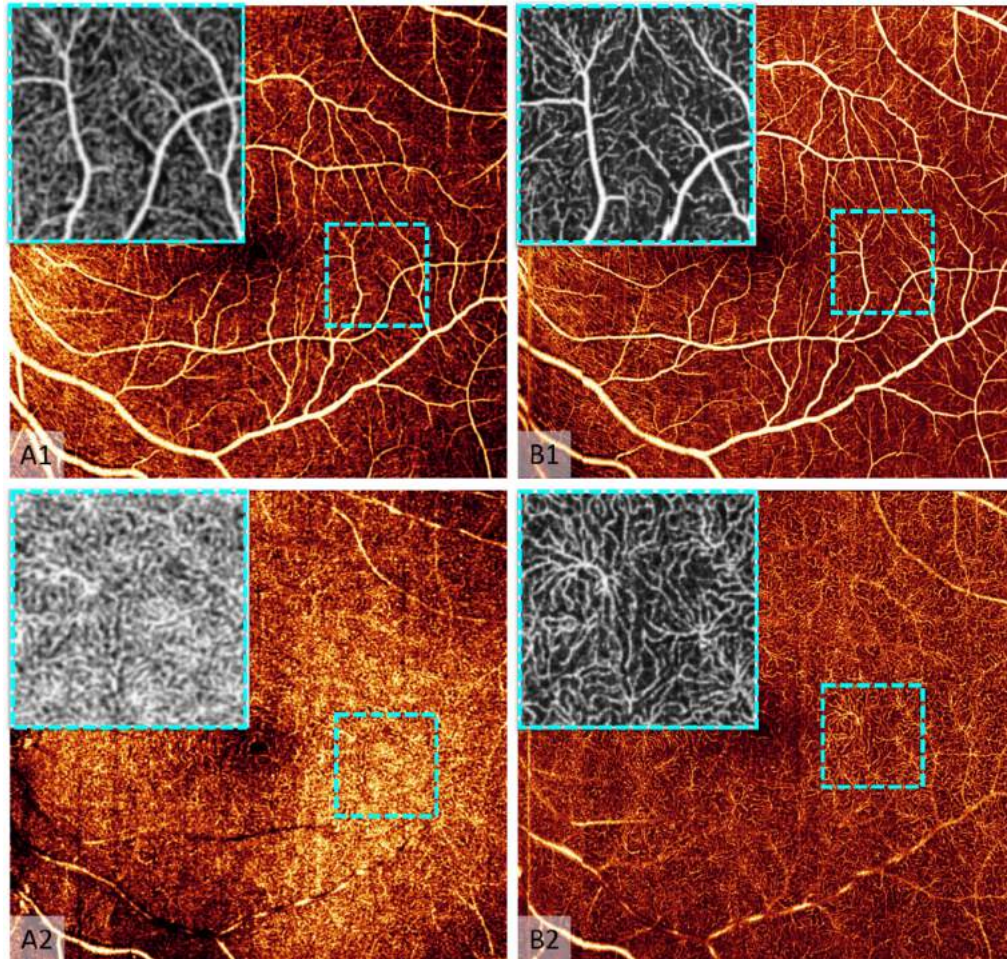


**Fig. 5. High transverse resolution is needed to accurately visualize and measure capillary details** from a healthy eye. *Column A.*  $9 \times 9$ -mm images of the superficial vascular complex (SVC; *row 1*) and deep capillary plexus (*row 2*) captured with a commercial device (Solix, Visionix, CA) and used a  $15 \mu\text{m}/\text{pixel}$  sampling density. *Column B.* The same eye captured with the custom device in this study using  $11.4 \mu\text{m}/\text{pixel}$  transverse sampling density. In both cases, flow signal was generated using split-spectrum amplitude decorrelation angiography (SSADA) from 3 repeats. Insets show magnifications of the region within the teal dotted box. While large vessels are clear throughout the SVC in images from both devices, in vascularly dense locations individual capillaries are difficult to trace, with the vasculature appearing like a sheet with just local variation in flow signal. This issue is exacerbated in the deep capillary plexus, where vessel shapes or connectivity are very difficult to assess in the commercial image. Images from the device in this study instead clearly reveal the lobular nature of the vessel patterns in this plexus.

**Low signal roll-off.** A combination of high transverse resolution imaging and deep signal penetration is essential for imaging the choriocapillaris (Fig. 6), which is implicated or speculated



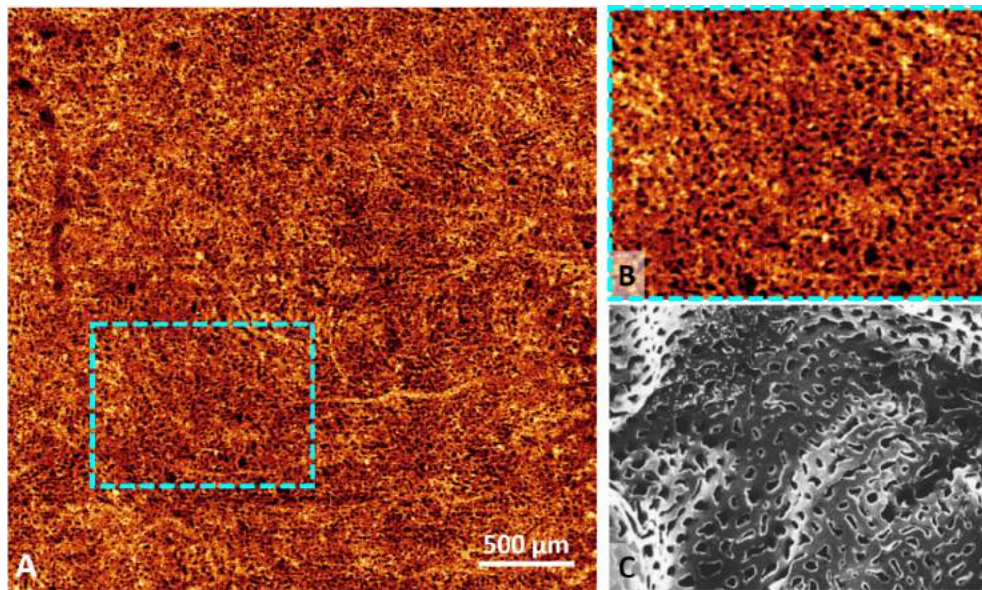


**Fig. 6. Histologic detail with OCT angiography.** (A)  $3 \times 3$ -mm en face OCT angiography (OCTA) of the central macula. (B) Blow-up of the region in the teal rectangle in (A) reveals the morphology of the vessels in this region, including flow gaps. (C) Scanning electron microscope image of the central macular choriocapillaris. The vascular patterns in (B) and (C) are visually similar, with the OCTA images revealing the fenestrated appearance shown in the histologic image. The histologic image was reproduced from Olver et. al with permission [45].

to play a role in the development of important retinal diseases [46,47]. However, signal attenuation usually prevents detailed visualization of the vasculature in the choriocapillaris. The choriocapillaris is beneath the retinal pigment epithelium, which strongly attenuates the reflectance signal. Low signal in the choriocapillaris is exacerbated beneath the macula due to the density of the overlying cone photoreceptors, which are tightly packed in this region, and vasculature as well as the relative thickness of the macular retina compared to more peripheral areas. In total these issues previously prevented the identification of individual capillary or intercapillary morphology in the macular choriocapillaris in healthy eyes. The combination of high transverse resolution and signal penetration in our system produces choriocapillaris images that recapitulate the main features visible with electron microscopy (which offers highest ex vivo resolution currently available; Fig. 6).

**Single-shot large-volume imaging.** While the transverse dimensions of the field of view in OCT imaging are more frequently discussed, the low signal roll-off in our system is also important for expanding the imaging volume (Fig. 4). Below (c.f. Figure 9) we give an example of peripheral deep tissue imaging that relies on both extended axial and transverse fields of view.

### 3.2. Study population

To assess the device's utility for medical imaging, we imaged 194 volunteers with age-related macular degeneration, 95 with diabetic retinopathy, and 10 with branch retinal vein occlusion. These diseases require different imaging priorities based on the disease specific features needed to describe severity and/or predict disease progression, and so together offer a useful means to assess our device's performance. We selected representative data from three healthy volunteers, one patient with AMD, two with DR, and one with BRVO.

### 3.3. Age-related macular degeneration

Age-related macular degeneration (AMD) is a major target for research in ophthalmology as it is a leading cause of blindness [1] with several aspects of its pathophysiology under investigation [45,48]. Permanent vision loss is associated with advanced AMD, characterized by the presence of geographic atrophy (GA) or the development of exudative AMD, the hallmark feature of which is the presence of choroidal neovascularization (CNV) [49]. Both OCT and OCTA are routinely used for diagnosis and management of advanced AMD [50,51]. Anti-vascular endothelial growth factor (anti-VEGF) therapies are a proven treatment for improving visual outcomes for eyes with exudative AMD [52,53]. However a significant number of eyes undergoing treatment for exudative AMD may lose vision due to the development of geographic atrophy [54,55]. Inhibition of complement C3 with intravitreal pegcetacoplan has been shown to slow GA growth; however, studies have not demonstrated visual benefit [56,57]. Therapy development for geographic atrophy, therefore, represents an exceptional clinical priority for ophthalmic research. Geographic atrophy is an advanced state of degeneration, in which photoreceptor cells and the retinal pigment epithelium are lost. Concurrent capillary loss in the choriocapillaris is also observed in geographic atrophy, but even basic questions such as whether choriocapillaris loss precedes retinal pigment epithelium loss are currently unresolved [58–60]. This is likely in part due to the difficulty of observing the choriocapillaris beneath the macula. The high density and small thickness of the choriocapillaris, in addition to diffuse dye leakage from leaky choriocapillaris vessels prevents visualization of fine vascular morphologic details with dye-based angiography [61,62]. Conventional OCTA has better resolution and choriocapillaris flow deficits can be detected [63]. These defects are useful because they predict geographic atrophy growth rate [64]. Deficits can be readily observed with our device (Fig. 7). Furthermore, because of

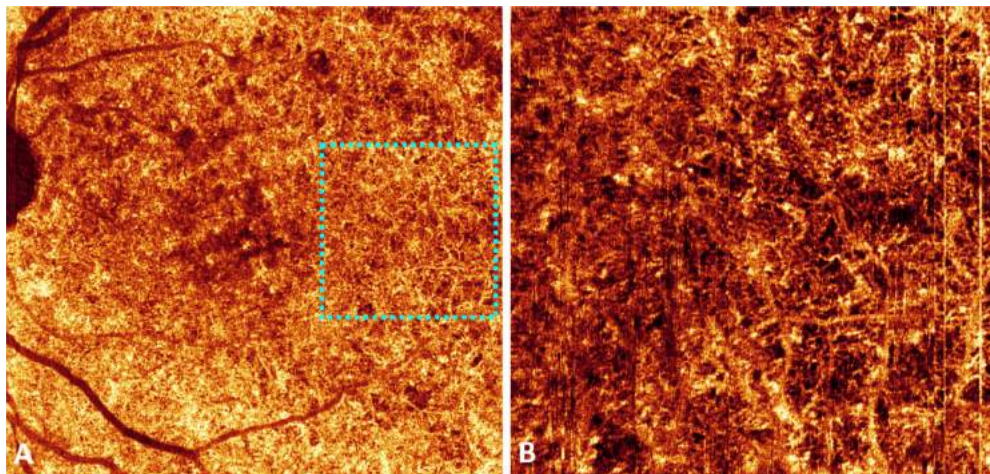


**Fig. 7. Choriocapillaris imaging in age-related macular degeneration.** (A) A  $9 \times 9$ -mm OCTA angiogram of the choriocapillaris. This  $9 \times 9$ -mm image was sampled at  $11.4 \mu\text{m}/\text{pixel}$  transverse density. (B)  $3 \times 3$ -mm scan at  $4 \mu\text{m}/\text{pixel}$  density of the region in the teal dotted square in (A). In the higher density scan individual capillary details can be ascertained, while defects and their margins can be clearly identified.

### 3.4. Diabetic retinopathy

Small transverse fields of view are perhaps the most recognized limitation of OCTA imaging. Conventional OCTA imaging often focuses on the macula or optic nerve head, but dye-based

angiography reveals that vascular pathology can present in the periphery [65–67]. However, because dye-based imaging is invasive, it cannot be used for routine clinical screening.

Furthermore, dye-based angiography may not detect some vascular pathology- for example, small neovascular vessels may be indistinguishable if they do not leak dye. OCTA can detect neovascularization missed by dye-based approaches [68]. OCTA therefore offers multiple potential advantages over dye-based angiography, but the inability of conventional devices to image the entire retina means that dye-based imaging is still required in some contexts.

Dye-based imaging is frequently used for the diagnosis and management of diabetic retinopathy (DR) [5]. Like AMD, DR is a leading cause of blindness [2]. Unlike AMD, important DR-related pathology such as neovascularization and non-perfusion area is not limited to the macula and often presents in the peripheral retina (Fig. 8). Vision threatening DR usually includes one or both of two important features: (1) diabetic macular edema, which is responsible for more vision loss than any other pathologic development in DR, and (2) retinal neovascularization, which is the defining feature of proliferative diabetic retinopathy (PDR) [69]. Effective treatment is available for both macular edema and PDR [5] but the disease must be detected at an early stage to achieve the best outcomes. High-resolution imaging is essential in characterizing macular edema and neovascular lesions, which can often be too small to be detected by clinical examination [70]. Since neovascular lesions may be present in the periphery (Fig. 8(A)), an ideal diagnostic modality must combine high-resolution with wide-field imaging.

There are other pathologic features in DR that can be used to stage the disease and predict progression [71]. Non-perfusion area is highly-correlated with DR severity and is amenable to quantification using OCTA [72–74]. But the conventional OCTA fields of view may not reveal the complete extent of the pathology (Fig. 7). We have demonstrated that quantification of nonperfusion area from larger fields of view improves correlation with DR stage [74]. There has been a growing recognition of DR that presents with predominantly peripheral lesions [75]. In the cases examined in this report, our device demonstrated extensive non-perfusion areas in the periphery. Hyperreflective foci, thought to be a sign of lipid extravasation in diabetic macular edema (Fig. 8(B)) [76] may precede the development of macular edema, and are associated with worse visual acuity [77] and visual outcomes with anti-VEGF [78–80]. Our device can image these with the structural channel and demonstrate their relationship with vascular features by visualizing them combined with an angiogram.

Microaneurysms are a key feature of DR that have not been consistently detected using commercial devices, with OCTA typically detecting fewer microaneurysms compared to fluorescein angiography due to the smaller field of view and the difference in the way vessels are identified (intrinsic motion contrast vs. exogenous fluorescent dye) [81]. OCTA, however, can determine the anatomic depth of the microaneurysms [11,12], and quantify the flow status in conjunction with high-resolution structural OCT [12]. With our device these features can be recognized in periphery, although we cannot comment on relative detection sensitivity in this work due to lacking corresponding fluorescein angiography images.

### 3.5. Branch retinal vein occlusion

The visualization of the peripheral retina is important in branch retinal vein occlusion (BRVO) [82], which is the most common retinal vascular disease after DR [3]. Non-perfusion area associated with BRVO may be peripheral and conventional OCTA with its small fields of view may not capture its full extent (Fig. 9). However, non-perfusion area measurements may be predictive of visual acuity outcomes and complication risks [83]. Simultaneously acquired coupled structural OCT can also demonstrate macular edema, which is the main cause of vision loss in BRVO [6].

Figure 9 shows an eye with BRVO imaged with our device. Prominent in the structural OCT channel in this eye are macrophage-like cells (MLC) visible as hyperreflective spots



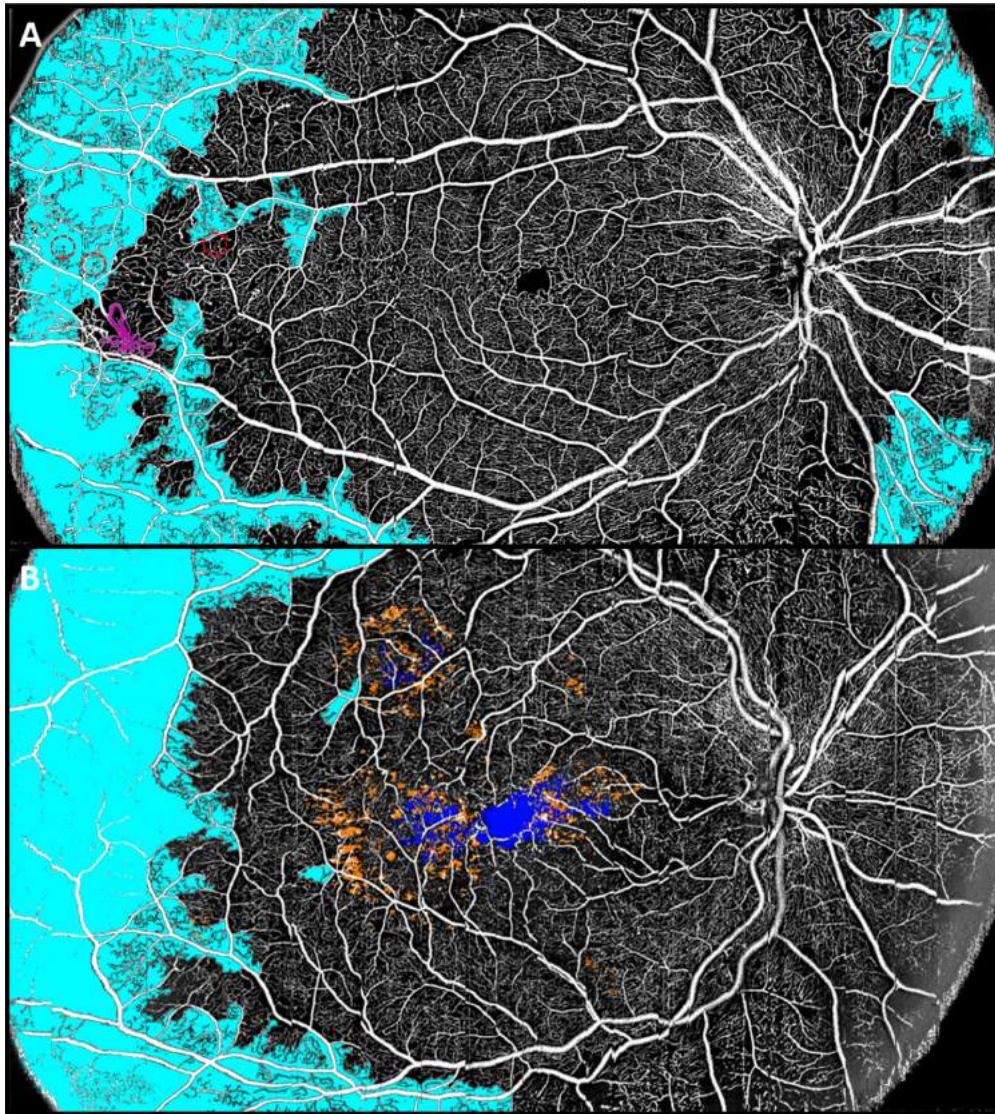


**Fig. 8. Wide-field imaging of multiple pathologic features in eyes with diabetic retinopathy (DR).** (A) A  $12 \times 23$ -mm en face image of the inner retina of an eye with proliferative DR shows extensive non-perfusion areas (teal), retinal neovascularization (purple; identified by its location anterior to the inner limiting membrane), and microaneurysms (red, circled) in the temporal periphery. (B) An eye with diabetic macular edema captured within the same field of view also reveals extensive non-perfusion area (teal). By combining with the structural image, lipid extravasation, which manifests as hyperreflective foci (orange), and retinal fluid (blue) can be imaged simultaneously. These  $12 \times 23$ -mm images were captured with  $10 \mu\text{m}/\text{pixel}$  transverse sampling density.

anterior to the internal limiting membrane (Fig. 9(A)). The MLCs are most likely vitreous cortex hyalocytes, which are believed to perform several functions including synthesis of structural proteins [84], immunological regulation [85], and modulation of inflammation [86]. They reside in the vitreous with high concentrations near the internal limiting membrane [87], although other macrophage lineages including microglia (in rats with induced ischemia) have also been described



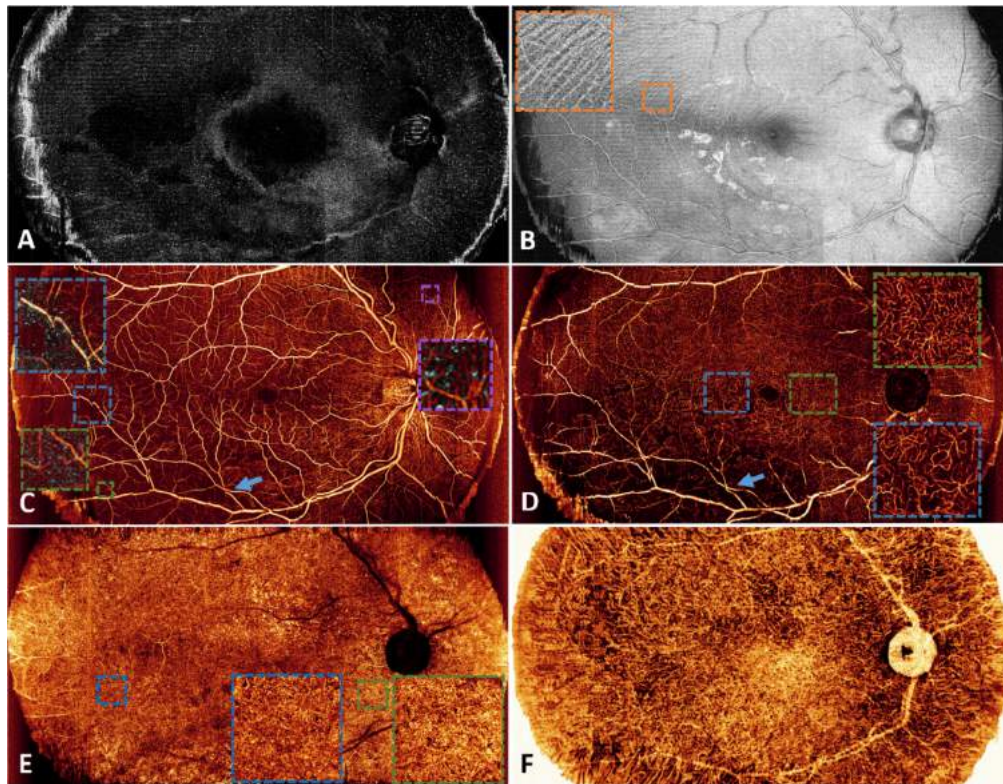


**Fig. 9. High-resolution, wide-field imaging of an eye with branch retinal vein occlusion.**

Throughout, color coded dotted boxes show magnifications of notable features. (A) A  $12 \times 23$ -mm structural image of the region extending from the inner limiting membrane  $10 \mu\text{m}$  into the vitreous. Macrophage-like cells can be identified as bright white dots. (B) Nerve fiber layer structural image. The magnification shows individual nerve fibers. (C) Superficial vascular complex angiogram. Here, the structural image showing macrophage-like cells is overlaid in teal. In the purple box, which is in an area unaffected by the vein occlusion, macrophage like cells appear evenly distributed, with no obvious correlation to the underlying vasculature. The same is true in a magnification of non-perfused area downstream of the occlusion (green box). However, in other locations the macrophage-like cells appear to cluster around vessels adjacent to non-perfusion areas (blue box). (D) Deep vascular complex angiogram. The non-perfused area appears larger in the deep vascular complex image (blue arrows in (C) and (D) at the same location for comparison). (E) Choriocapillaris angiogram. Magnifications of the regions in the blue and green boxes show similar intercapillary spacing in both the region of the eye afflicted by the vein occlusion (blue box) and in a region with healthy perfusion in the more superficial layers (green box). (F) In Sattler's layer it is also difficult to observe clear pathology in the region of the occlusion. These  $12 \times 23$ -mm image was captured with  $10 \mu\text{m}/\text{pixel}$  transverse sampling density.

histologically [88,89]. Previous OCT studies identified the hyperreflective spots anterior to the internal limiting membrane as MLCs based on observed translocation, inferred migration and/or apparent ramified morphology [33,90,91]. In this eye MLCs were observed to cluster near larger vessels in the areas of nonperfusion. This concurs with Ong et al., who found that OCT-detected MLCs in DR eyes were less likely than chance to be found co-localized with non-perfusion area [91]. A high-resolution and wide-field OCTs along with OCTA may help further elucidate the role of the MLCs in retinal vascular disorders (Fig. 9(C)).

The angiogram of the superficial and deep vascular complexes reveal non-perfusion area and telangiectasia with those changes being more prominent in the deeper slab. In particular, the capillary dropout appears more complete in the deep vascular plexus, and the non-perfusion area appears somewhat larger. Increased vessel tortuosity is also more apparent in this layer (Fig. 9(C), (D)). By contrast, there is no readily apparent difference in the region beneath the location of the occlusion in the choriocapillaris or Sattler's layer of the choroid (Fig. 9(E)).

#### 4. Discussion

The major limitation in conventional OCTA is the trade-off between sampling density and the size of the imaging volume. In most devices, this trade-off leads to either a lower image resolution or a limited field of view because imaging procedure times must be restricted to prevent eye motion from degrading image quality. The comprehensive imaging of retinal vessels and choroid presented here was achieved through a number of design features in a custom-built OCT/OCTA device. A critical component in this device is the 500-kHz swept source light source that seeks to avoid the field of view vs. resolution trade-off chiefly through increasing acquisition speed to a rate that allows sampling at high density across a larger part of the eye. It should be noted that this acquisition speed increase is not simply a matter of increasing laser sweep rates. Faster lasers are available (e.g. Fourier domain mode locked lasers can reach MHz A-line acquisition rates) but these light sources typically cannot achieve the same sensitivity as our device [92], which means that more points must be sampled to achieve the same resolution shown in this work. Since our goal is ultimately high-resolution imaging within an acceptable procedure time, laser choice is something of a design liberty. However, the improved sensitivity in our system is advantageous for imaging deeper layers such as the choriocapillaris, as we demonstrate in this work (Fig. 6,7).

The light source is not the only relevant component in our system design. Several other hardware components (including an optical relay to avoid vignetting, a reduced beam spot size to achieve optical resolution sufficient to image capillaries with minimal broadening, a self-tracking system to compensate for eye motion, and GPU-enabled real-time OCTA display for operator feedback) and software components (volumetric projection artifact removal and deep learning aided capillary reconstruction to denoise images) were required to achieve the images in this report.

Our device uses a single-shot procedure, but this is not the only means of achieving wide-field images. Another common strategy is to stitch several smaller field-of-view images together in order to construct a larger image [93–95]. Relative to a single shot procedure, montage can be implemented with less hardware investment and is consequently the preferred approach for most commercial devices attempting to achieve widefield imaging. However, this approach is impractical for clinical needs. Montage procedures increase the procedure time by multiplying the required number of scans. Even outside of time considerations, montage can be difficult to perform in a clinical environment due to patient inability to fixate. This difficulty leads to low image quality, which is a problem also in research environments. Alternatively, single-shot procedures do not require eccentric fixation, which means that they can improve image quality especially of eyes with low vision, which are often the eyes we want to image.

In the examples in this report, we demonstrated that several pathologic features (non-perfusion area, retinal neovascularization, photoreceptor and choriocapillaris loss, and retinal vein occlusion) associated with different diseases that required high resolution and signal penetration within an extended imaging volume in order to observe. The ability to detect small pathologic features throughout the retina and choroid non-invasively would improve our ability to characterize disease through different stages. First, this allows detection of pathologic features that may not be visible to the clinicians, such as small neovascularization or nonperfusion areas. Second, the larger field of view captures clinically significant pathology outside the conventional OCTA



field of view (Fig. 8,9). Most OCT imaging systems would require an extended imaging session with multiple volume acquisitions to capture all of the same details, and as such acquiring such detailed data is not currently clinically feasible. By avoiding complicated procedures in favor of a single shot approach our method represents a framework that could be adapted for clinical imaging.

The advantage of our approach is not limited to just detecting more of the same pathology typically observed with structural OCT and OCTA but in more places. We were also able to image features that have heretofore proven difficult to visualize with a single shot procedure. High-resolution imaging in combination with sensitive flow detection was able to clearly visualize individual capillary segments in the choriocapillaris, and in particular in the macular region (Fig. 6). The choriocapillaris likely plays a key role in AMD pathogenesis [46,96], but the inability to image the choriocapillaris below the macula in vivo has limited our ability to investigate an etiological relationship. Conventional OCTA can detect flow deficits [97], but capillary details are lacking, preventing precise quantification of other possible metrics (for example, metrics based on vessel morphology). That capillary details can be visualized using our approach leads to the possibility that novel choriocapillaris features could be quantified and used to stage AMD or improve prediction of developing pathology. We were also able to obtain images of macrophage-like cells in the vitreous (Fig. 9). These cells are a key component of the inflammatory immune response in the eye [85,86,98], but either enhanced resolution such as that provided by the device in this report or multiple image averaging [33,91] are required to image them. However, compared to multiple image averaging in commercial devices, our approach has the additional advantage of being able to image macrophage-like cell imaging in the periphery (Fig. 9(A), (C)), allowing a more complete investigation of its role in various diseases.

In total, then, our approach is able to image both novel features such as macrophage-like cells and macular choriocapillaris vascular anatomy as well as more maturely characterized pathologic features (e.g. non-perfusion area) simultaneously throughout a large region of the retina and choroid. Simultaneous imaging of multiple pathologic features (Fig. 7,8) allows inter-relationships between such features to be explored. This will be key to understanding the role that novel biomarkers could play in clinical practice or in explaining disease mechanisms. Finally, the ability to simultaneously characterize pathologic structural and vascular detail can enhance feature detection itself [12]. The comprehensive imaging provided by the next generation of high-speed OCT devices, of which our prototype is an example, offers the possibility of a more complete characterization of disease pathophysiology and etiology, which could ultimately improve our ability to generate new therapeutic targets and treatments.

There are limitations in the current work. We did not quantify any of the features that we visualized in the current report, which means that we cannot comment on whether we can achieve reliable measurement particularly of the more novel structures we imaged. There is also image quality variation apparent in the images in our report between the macula/image center and the periphery (Fig. 8,9). Much of this is due to aberration in the eye, which could be corrected with adaptive optics. We did not pursue this approach here, since we envision this work as striving toward a clinical imaging approach for which adaptive optics is not currently feasible. However, this is still an optical improvement that could be considered.

## 5. Conclusion

Coupled structural OCT and OCT angiography can characterize several important features in multiple diseases. Because it obtains both high-resolution and volumetric data for some of these features, OCT is considered a gold standard approach for detection and is used in preferred practice. We presented a swept-source device that provides high-sensitivity, high-resolution imaging in an extended imaging volume in order to identify biomarkers throughout the macula, optic nerve head, and peripheral retina using a single-shot procedure. With enhanced depth

penetration from the swept source wavelength and hardware and software approaches to correct imaging artifacts, our device can also image choroidal circulation throughout the same field of view. By relying on a single-shot approach, we ensured that our approach is practical for large-scale imaging projects and could be adapted for clinical practice. In addition to conventional structural OCT and OCTA biomarkers, we were also able to image macrophage-like cells above the inner limiting membrane and choriocapillaris vessels beneath the macula, both of which are difficult to visualize with contemporary commercial devices but may still be important to analyze in order to achieve a more complete understanding of etiology.

**Funding.** Bright Focus Foundation (G2020168, M20230081); Edward N. & Della L. Thome Memorial Foundation Award; Dr. H. James and Carole Free Catalyst Award from Research to Prevent Blindness; Malcolm M. Marquis, MD Endowed Fund for Innovation; National Institutes of Health (P30 EY010572, R01 EY023285, R01 EY024544, R01 EY027833, R01 EY031394, R01 EY035410, T32 EY023211, UL1TR002369).

**Acknowledgments.** This work was supported by the National Institute of Health (R01 EY027833, R01 EY035410, R01 EY024544, R01 EY031394, R01 EY023285, T32 EY023211, UL1TR002369, P30 EY010572); the Malcolm M. Marquis, MD Endowed Fund for Innovation; an Unrestricted Departmental Funding Grant and Dr. H. James and Carole Free Catalyst Award from Research to Prevent Blindness (New York, NY), Edward N. & Della L. Thome Memorial Foundation Award, and the Bright Focus Foundation (G2020168, M20230081).

**Disclosures.** Yukun Guo: Optovue/Visionix, Inc (P), Genentech, Inc (P); Jie Wang: Optovue/Visionix, Inc (P, R), Genentech, Inc (P); David Huang: Optovue/Visionix, Inc. (F, P, R), Boeringer Ingelheim (C); Yali Jia: Optovue/Visionix, Inc. (P, R), Optos (P), Genentech, Inc (P, F). These potential conflicts of interest have been reviewed and managed by OHSU. Other authors declare no conflicts of interest related to this article.

**Data availability.** Data underlying the results presented in this paper are not publicly available at this time but may be obtained from the authors upon reasonable request.

## References

- W. L. Wong, X. Su, X. Li, *et al.*, "Global prevalence of age-related macular degeneration and disease burden projection for 2020 and 2040: A systematic review and meta-analysis," *Lancet Glob. Heal.* **2**(2), e106–e116 (2014).
- Z. L. Teo, Y. C. Tham, M. Yu, *et al.*, "Global Prevalence of Diabetic Retinopathy and Projection of Burden through 2045: Systematic Review and Meta-analysis," *Ophthalmology* **128**(11), 1580–1591 (2021).
- P. Song, Y. Xu, M. Zha, *et al.*, "Global epidemiology of retinal vein occlusion: A systematic review and meta-analysis of prevalence, incidence, and risk factors," *J. Glob. Health* **9**(1), 1 (2019).
- C. J. Flaxel, R. A. Adelman, S. T. Bailey, *et al.*, "Age-Related Macular Degeneration Preferred Practice Pattern®," *Ophthalmology* **127**(1), P1–P65 (2020).
- C. J. Flaxel, R. A. Adelman, S. T. Bailey, *et al.*, "Diabetic Retinopathy Preferred Practice Pattern," *Ophthalmology* **127**(1), P66–P145 (2020).
- J. S. Pulido, C. J. Flaxel, R. A. Adelman, *et al.*, "Retinal Vein Occlusions Preferred Practice Pattern," *Ophthalmology* **123**(1), P182–P208 (2016).
- J. F. Russell, H. W. Flynn, J. Sridhar, *et al.*, "Distribution of Diabetic Neovascularization on Ultra-Widefield Fluorescein Angiography and on Simulated Widefield OCT Angiography," *Am. J. Ophthalmol.* **207**, 110–120 (2019).
- K. Tsuboi, Y. Ishida, T. Wakabayashi, *et al.*, "Presumed Glial Sprouts as a Predictor of Preretinal Neovascularization in Retinal Vein Occlusion," *JAMA Ophthalmol.* **140**(3), 284–285 (2022).
- K. Tsuboi, M. Mazloumi, Y. Guo, *et al.*, "Utility of En face OCT for the Detection of Clinically Unsuspected Retinal Neovascularization in Patients with Diabetic Retinopathy," *Ophthalmol. Retin.* **7**(8), 683–691 (2023).
- V. Schreur, A. Domanian, B. Liefers, *et al.*, "Morphological and topographical appearance of microaneurysms on optical coherence tomography angiography," *Br. J. Ophthalmol.* **103**(5), 630–635 (2019).
- E. Borrelli, R. Sacconi, M. Brambati, *et al.*, "In vivo rotational three-dimensional OCTA analysis of microaneurysms in the human diabetic retina," *Sci. Rep.* **9**(1), 1–8 (2019).
- M. Gao, T. T. Hormel, Y. Guo, *et al.*, "Active and inactive microaneurysms identified and characterized by structural and angiographic optical coherence tomography," *arXiv*, arXiv:2303.13611 (2023).
- D. Huang, E. A. Swanson, C. P. Lin, *et al.*, "Optical Coherence Tomography," *Science* **254**(5035), 1178–1181 (1991).
- J. Fujimoto and E. Swanson, "The development, commercialization, and impact of optical coherence tomography," *Investig. Ophthalmol. Vis. Sci.* **57**(9), OCT1–OCT13 (2016).
- Q. S. You, K. Tsuboi, Y. Guo, *et al.*, "Comparison of Central Macular Fluid Volume with Central Subfield Thickness in Patients with Diabetic Macular Edema Using Optical Coherence Tomography Angiography," *JAMA Ophthalmol.* **139**(7), 734–741 (2021).
- L. de Sisternes, N. Simon, R. Tibshirani, *et al.*, "Quantitative SD-OCT imaging biomarkers as indicators of age-related macular degeneration progression," *Investig. Ophthalmol. Vis. Sci.* **55**(11), 7093–7103 (2014).
- U. Schmidt-Erfurth and S. M. Waldstein, "A paradigm shift in imaging biomarkers in neovascular age-related macular degeneration," *Prog. Retin. Eye Res.* **50**, 1–24 (2016).

18. S. Farsiu, S. J. Chiu, R. V. O'Connell, *et al.*, "Quantitative classification of eyes with and without intermediate age-related macular degeneration using optical coherence tomography," *Ophthalmology* **121**(1), 162–172 (2014).
19. T. Otani, S. Kishi, and Y. Maruyama, "Patterns of Diabetic Macular Edema With Optical Coherence Tomography," *Am. J. Ophthalmol.* **127**(6), 688–693 (1999).
20. Diabetic Retinopathy Clinical Research Network, "The Relationship between OCT-measured Central Retinal Thickness and Visual Acuity in Diabetic Macular Edema," *Ophthalmology* **114**(3), 525–536 (2007).
21. G. Virgili, F. Menchini, G. Casazza, *et al.*, "Optical coherence tomography (OCT) for detection of macular oedema in patients with diabetic retinopathy," *Cochrane Database Syst. Rev.* **2015**, 1–57 (2015).
22. S. Makita, Y. Hong, M. Yamanari, *et al.*, "Optical coherence angiography," *Opt. Express* **14**(17), 7821–7840 (2006).
23. L. An and R. K. Wang, "In vivo volumetric imaging of vascular perfusion within human retina and choroids with optical micro-angiography," *Opt. Express* **16**(15), 11438–11452 (2008).
24. Y. Jia, O. Tan, J. Tokayer, *et al.*, "Split-spectrum amplitude-decorrelation angiography with optical coherence tomography," *Opt. Express* **20**(4), 4710–4725 (2012).
25. R. F. Spaide, J. G. Fujimoto, N. K. Waheed, *et al.*, "Optical coherence tomography angiography," *Prog. Retin. Eye Res.* **64**, 1–55 (2018).
26. T. T. Hormel, Y. Jia, Y. Jian, *et al.*, "Plexus-specific retinal vascular anatomy and pathologies as seen by projection-resolved optical coherence tomographic angiography," *Prog. Retin. Eye Res.* **80**, 100878 (2021).
27. T. T. Hormel, D. Huang, and Y. Jia, "Artifacts and artifact removal in optical coherence tomographic angiography," *Quant Imaging Med Surg.* **11**(3), 1120–1133 (2020).
28. M. Zhang, T. S. Hwang, J. P. Campbell, *et al.*, "Projection-resolved optical coherence tomographic angiography," *Biomed. Opt. Express* **7**(3), 816–828 (2016).
29. X. Wei, T. T. Hormel, and Y. Jia, "Phase-stabilized complex-decorrelation angiography," *Biomed. Opt. Express* **12**(4), 2419–2431 (2021).
30. X. Wei, T. T. Hormel, Y. Guo, *et al.*, "75-degree non-mydratic single-volume optical coherence tomographic angiography," *Biomed. Opt. Express* **10**(12), 6286–6295 (2019).
31. A. Uji, S. Balasubramanian, J. Lei, *et al.*, "Choriocapillaris imaging using multiple en face optical coherence tomography angiography image averaging," *JAMA Ophthalmol.* **135**(11), 1197–1204 (2017).
32. Q. Zhang, F. Zheng, E. H. Motulsky, *et al.*, "A novel strategy for quantifying choriocapillaris flow voids using swept-source OCT angiography," *Investig. Ophthalmol. Vis. Sci.* **59**(1), 203–211 (2018).
33. M. V. Castanos, D. B. Zhou, R. E. Linderman, *et al.*, "Imaging of macrophage-like cells in living human retina using clinical OCT," *Investig. Ophthalmol. Vis. Sci.* **61**, 1 (2020).
34. *American National Standard for Safe Use of Lasers (ANSI Z136.1-2014)* (2014).
35. X. Wei, T. T. Hormel, S. Pi, *et al.*, "Wide-field sensorless adaptive optics swept-source optical coherence tomographic angiography in rodents," *Opt. Lett.* **47**(19), 5060 (2022).
36. M. Wojtkowski, V. J. Srinivasan, T. H. Ko, *et al.*, "Domain Optical Coherence Tomography and," *Opt. Express* **12**(11), 2404 (2004).
37. K. Shimizu and K. Ujiie, *Structure of Ocular Vessels* (Igaku-Shoin Ltd., 1978).
38. S. S. Hayreh, "Vascular pattern of the choriocapillaris," *Exp. Eye Res.* **19**(1), 101–104 (1974).
39. Y. Guo, A. Camino, M. Zhang, *et al.*, "Automated segmentation of retinal layer boundaries and capillary plexuses in wide-field optical coherence tomographic angiography," *Biomed. Opt. Express* **9**(9), 4429–4442 (2018).
40. T. T. Hormel, J. Wang, S. T. Bailey, *et al.*, "Maximum value projection produces better en face OCT angiograms than mean value projection," *Biomed. Opt. Express* **9**(12), 6412–6424 (2018).
41. X. Wei, T. T. Hormel, Y. Guo, *et al.*, "High-resolution wide-field OCT angiography with a self-navigation method to correct microsaccades and blinks," *Biomed. Opt. Express* **11**(6), 3234 (2020).
42. J. Wang, T. T. Hormel, S. T. Bailey, *et al.*, "Signal attenuation-compensated projection-resolved OCT angiography," *Biomed. Opt. Express* **14**(5), 2040–2054 (2023).
43. M. Gao, T. T. Hormel, J. Wang, *et al.*, "An open-source deep learning network for reconstruction of high-resolution oct angiograms of retinal intermediate and deep capillary plexuses," *Transl. Vis. Sci. Technol.* **10**(13), 13 (2021).
44. P. L. Nesper and A. A. Fawzi, "Human parafoveal capillary vascular anatomy and connectivity revealed by optical coherence tomography angiography," *Investig. Ophthalmol. Vis. Sci.* **59**(10), 3858–3867 (2018).
45. S. Mehta, "Age-related macular degeneration," *Lancet* **392**(10153), 1147–1159 (2018).
46. Philip J. Rosenfeld, Omer Trivizki, Giovanni Gregori, *et al.*, "An Update on the Hemodynamic Model of Age-Related Macular Degeneration," *Am. J. Ophthalmol.* **235**, 291–299 (2022).
47. E. J. Duh, J. K. Sun, and A. W. Stitt, "Diabetic retinopathy: current understanding, mechanisms, and treatment strategies," *JCI Insight* **2**(14), 1–13 (2017).
48. R. Flores, A. Carneiro, M. Vieira, *et al.*, "Age-Related Macular Degeneration: Pathophysiology, Management, and Future Perspectives," *Ophthalmologica* **244**(6), 495–511 (2021).
49. F. L. Ferris, C. P. Wilkinson, A. Bird, *et al.*, "Clinical classification of age-related macular degeneration," *Ophthalmology* **120**(4), 844–851 (2013).
50. A. Faridi, Y. Jia, S. S. Gao, *et al.*, "Sensitivity and Specificity of OCT Angiography to Detect Choroidal Neovascularization," *Ophthalmol. Retin.* **1**(4), 294–303 (2017).
51. S. R. Sadda, R. Guymer, F. G. Holz, *et al.*, "Consensus Definition for Atrophy Associated with Age-Related Macular Degeneration on OCT: Classification of Atrophy Report 3," *Ophthalmology* **125**(4), 537–548 (2018).



52. J. S. Heier, D. M. Brown, V. Chong, *et al.*, "Intravitreal aflibercept (VEGF trap-eye) in wet age-related macular degeneration," *Ophthalmology* **119**(12), 2537–2548 (2012).
53. D. M. Brown, P. K. Kaiser, M. Michels, *et al.*, "Ranibizumab versus verteporfin for neovascular age-related macular degeneration," *N. Engl. J. Med.* **355**(14), 1432–1444 (2006).
54. J. E. Grunwald, M. Pistilli, E. Daniel, *et al.*, "Incidence and Growth of Geographic Atrophy during 5 Years of Comparison of Age-Related Macular Degeneration Treatments Trials," *Ophthalmology* **124**(1), 97–104 (2017).
55. S. Rofagha, R. B. Bhisitkul, D. S. Boyer, *et al.*, "Seven-year outcomes in ranibizumab-treated patients in ANCHOR, MARINA, and HORIZON: A multicenter cohort study (SEVEN-UP)," *Ophthalmology* **120**(11), 2292–2299 (2013).
56. R. Goldberg, J. S. Heier, C. C. Wykoff, *et al.*, "Efficacy of intravitreal pegcetacoplan in patients with geographic atrophy (GA): 12-month results from the phase 3 OAKS and DERBY studies," *Invest. Ophthalmol. Vis. Sci.* **63**, 1500 (2022).
57. D. S. Liao, F. V. Grossi, D. El Mehdi, *et al.*, "Complement C3 Inhibitor Pegcetacoplan for Geographic Atrophy Secondary to Age-Related Macular Degeneration: A Randomized Phase 2 Trial," *Ophthalmology* **127**(2), 186–195 (2020).
58. D. S. Mcleod, R. Grebe, I. Bhutto, *et al.*, "Relationship between RPE and choriocapillaris in age-related macular degeneration," *Investig. Ophthalmol. Vis. Sci.* **50**(10), 4982–4991 (2009).
59. E. H. Sohn, M. J. Flamme-Wiese, S. S. Whitmore, *et al.*, "Choriocapillaris Degeneration in Geographic Atrophy," *Am. J. Pathol.* **189**(7), 1473–1480 (2019).
60. R. S. Ramrattan, T. L. Van der Schaft, C. M. Mooy, *et al.*, "Morphometric analysis of Bruch's membrane, the choriocapillaris, and the choroid in aging," *Investig. Ophthalmol. Vis. Sci.* **35**, 2857–2864 (1994).
61. D. P. Pauleikhoff, G. Spital, M. Radermacker, *et al.*, "A fluorescein and indocyanine green angiographic study of choriocapillaris in age - related macular degeneration," *Evidence-Based Eye Care* **1**(2), 92–93 (2000).
62. R. Forte, G. Querques, L. Querques, *et al.*, "Multimodal imaging of dry age-related macular degeneration," *Acta Ophthalmol.* **90**, 281–287 (2012).
63. E. Borrelli, D. Sarraf, K. B. Freund, *et al.*, "OCT angiography and evaluation of the choroid and choroidal vascular disorders," *Prog. Retin. Eye Res.* **67**, 30–55 (2018).
64. Q. S. You, A. Camino, J. Wang, *et al.*, "Geographic Atrophy Progression Is Associated With Choriocapillaris Flow Deficits Measured With Optical Coherence Tomographic Angiography," *Investig. Ophthalmol. Vis. Sci.* **62**(3), 1–7 (2021).
65. P. S. Silva, J. D. Cavallerano, N. M. N. Haddad, *et al.*, "Peripheral lesions identified on ultrawide field imaging predict increased risk of diabetic retinopathy progression over 4 years," *Ophthalmology* **122**(5), 949–956 (2015).
66. P. S. Silva, J. D. Cavallerano, J. K. Sun, *et al.*, "Peripheral lesions identified by mydriatic ultrawide field imaging: Distribution and potential impact on diabetic retinopathy severity," *Ophthalmology* **120**(12), 2587–2595 (2013).
67. P. S. Silva, A. J. Dela Cruz, M. G. Ledesma, *et al.*, "Diabetic retinopathy severity and peripheral lesions are associated with nonperfusion on ultrawide field angiography," *Ophthalmology* **122**(12), 2465–2472 (2015).
68. Q. S. You, Y. Guo, J. Wang, *et al.*, "Detection of Clinically Unsuspected Retinal Neovascularization With Wide-Field Optical Coherence Tomography Angiography," *Retina* **40**(5), 891 (2020).
69. R. Lee, T. Y. Wong, and C. Sabanayagam, "Epidemiology of diabetic retinopathy, diabetic macular edema and related vision loss," *Eye Vis.* **2**(1), 17 (2015).
70. A. Ishibazawa, T. Nagaoka, H. Yokota, *et al.*, "Characteristics of retinal neovascularization in proliferative diabetic retinopathy imaged by optical coherence tomography angiography," *Investig. Ophthalmol. Vis. Sci.* **57**(14), 6247–6255 (2016).
71. A. W. Stitt, T. M. Curtis, M. Chen, *et al.*, "The progress in understanding and treatment of diabetic retinopathy," *Prog. Retin. Eye Res.* **51**, 156–186 (2016).
72. T. S. Hwang, A. M. Hagag, J. Wang, *et al.*, "Automated quantification of nonperfusion areas in 3 vascular plexuses with optical coherence tomography angiography in eyes of patients with diabetes," *JAMA Ophthalmol.* **136**(8), 929–936 (2018).
73. M. Zhang, T. S. Hwang, C. Dongye, *et al.*, "Automated quantification of nonperfusion in three retinal plexuses using projection-resolved optical coherence tomography angiography in diabetic retinopathy," *Investig. Ophthalmol. Vis. Sci.* **57**(13), 5101–5106 (2016).
74. Y. Guo, T. T. Hormel, L. Gao, *et al.*, "Quantification of Nonperfusion Area in Montaged Widefield OCT Angiography Using Deep Learning in Diabetic Retinopathy," *Ophthalmol. Sci.* **1**(2), 100027 (2021).
75. D. M. Marcus, P. S. Silva, D. Liu, *et al.*, "Association of Predominantly Peripheral Lesions on Ultra-Widefield Imaging and the Risk of Diabetic Retinopathy Worsening over Time," *JAMA Ophthalmol.* **140**(10), 946–954 (2022).
76. R.-A. P., B.-B. M., P.-R. A., L.-G. M., N.-G. R., and P. O. Verges R. AO - Romero-Aroca, "Diabetic Macular Edema Pathophysiology: Vasogenic versus Inflammatory," *J. Diabetes Res.* **2016**, 1–17 (2016).
77. T. Horii, A. Uji, Y. Muraoka, *et al.*, "Association Between Hyperreflective Foci in the Outer Retina, Status of Photoreceptor Layer, and Visual Acuity in Diabetic Macular Edema," *Am. J. Ophthalmol.* **153**(4), 710–717.e1 (2012).
78. J. Kang, H. Chung, and H. C. Kim, "Correlation of Optical Coherence Tomographic Hyperreflective Foci with Visual Outcomes in Different Patterns of Diabetic Macular Edema," *Retina* **36**(9), 1630–1639 (2016).
79. S. Vujosevic, M. Berton, S. Bini, *et al.*, "Hyperreflective retinal spots and visual function after anti-vascular endothelial growth factor treatment in center-involving diabetic macular edema," *Retina* **36**(7), 1298–1308 (2016).

80. R. Sacconi, R. Lattanzio, L. Pierro, *et al.*, "Optical Coherence Tomographic Hyperreflective Foci in Early Stages of Diabetic Retinopathy," *Retina* **35**(3), 449–453 (2015).
81. S. Parrulli, F. Corvi, M. Cozzi, *et al.*, "Microaneurysms visualisation using five different optical coherence tomography angiography devices compared to fluorescein angiography," *Br. J. Ophthalmol.* **105**(4), 526–530 (2021).
82. S. S. Hayreh, M. B. Zimmerman, and P. Podhajsky, "Incidence of various types of retinal vein occlusion and their recurrence and demographic characteristics," *Am. J. Ophthalmol.* **117**(4), 429–441 (1994).
83. N. L. B. Christoffersen and M. Larsen, "Pathophysiology and hemodynamics of branch retinal vein occlusion," *Ophthalmology* **106**(11), 2054–2062 (1999).
84. S. K. Boneva, J. Wolf, D. D. Rosmus, *et al.*, "Transcriptional Profiling Uncovers Human Hyalocytes as a Unique Innate Immune Cell Population," *Front. Immunol.* **11**, 1–14 (2020).
85. S. K. Boneva, J. Wolf, P. Wieghofer, *et al.*, "Hyalocyte functions and immunology," *Expert Rev. Ophthalmol.* **17**(4), 249–262 (2022).
86. T. Kita, Y. Hata, and T. Ishibashi, "Hyalocytes: Essential Cells of the Vitreous Cavity in Vitreoretinal Pathophysiology?" *Encycl. Eye* **1**, 251–256 (2010).
87. N. N. Vagaja, H. R. Chinnery, N. Binz, *et al.*, "Changes in murine hyalocytes are valuable early indicators of ocular disease," *Investig. Ophthalmol. Vis. Sci.* **53**(3), 1445–1451 (2012).
88. E. G. O'Koren, C. Yu, M. Klingeborn, *et al.*, "Microglial Function Is Distinct in Different Anatomical Locations during Retinal Homeostasis and Degeneration," *Immunity* **50**(3), 723–737.e7 (2019).
89. C. Zhang, T. T. Lam, and M. O. Tso, "Heterogeneous populations of microglia/macrophages in the retina and their activation after retinal ischemia and reperfusion injury," *Exp. Eye Res.* **81**(6), 700–709 (2005).
90. D. X. Hammer, A. Agrawal, R. Villanueva, *et al.*, "Label-free adaptive optics imaging of human retinal macrophage distribution and dynamics," *Proc. Natl. Acad. Sci. U. S. A.* **117**(48), 30661–30669 (2020).
91. J. X. Ong, P. L. Nesper, A. A. Fawzi, *et al.*, "Macrophage-like cell density is increased in proliferative diabetic retinopathy characterized by optical coherence tomography angiography," *Investig. Ophthalmol. Vis. Sci.* **62**(10), 2 (2021).
92. A. Agrawal, T. J. Pfefer, P. D. Woolliams, *et al.*, "Methods to assess sensitivity of optical coherence tomography systems," *Biomed. Opt. Express* **8**(2), 902 (2017).
93. F. P. Wang, S. S. Saraf, Q. Zhang, *et al.*, "Ultra-Widefield Protocol Enhances Automated Classification of Diabetic Retinopathy Severity with OCT Angiography," *Ophthalmol. Retin.* **4**(4), 415–424 (2020).
94. J. Wang, A. Camino, X. Hua, *et al.*, "Invariant features-based automated registration and montage for wide-field OCT angiography," *Biomed. Opt. Express* **10**(1), 120–136 (2019).
95. M. Niederleithner, L. De Sisternes, H. Stino, *et al.*, "Ultra-widefield OCT Angiography," *IEEE Trans. Med. Imaging* **42**(4), 1009–1020 (2023).
96. A. Swaroop, E. Y. Chew, C. B. Rickman, *et al.*, "Unraveling a multifactorial late-onset disease: From genetic susceptibility to disease mechanisms for age-related macular degeneration," *Annu. Rev. Genomics Hum. Genet.* **10**(1), 19–43 (2009).
97. A. Camino, Y. Guo, Q. You, *et al.*, "Detecting and measuring areas of choriocapillaris low perfusion in intermediate, non-neovascular age-related macular degeneration," *Neurophotonics* **6**(04), 1 (2019).
98. C. H. Jones, W. Gui, R. G. Schumann, *et al.*, "Hyalocytes in proliferative vitreo-retinal diseases," *Expert Rev. Ophthalmol.* **17**(4), 263–280 (2022).